Bacteria Single-Cell and Photosensitizer Interaction

Subjects: Microbiology
Contributor: Igor Buzalewicz

Quantifying changes in bacteria cells in the presence of antibacterial treatment is one of the main challenges facing contemporary medicine; it is a challenge that is relevant for tackling issues pertaining to bacterial biofilm formation that substantially decreases susceptibility to biocidal agents. Three-dimensional label-free imaging and quantitative analysis of bacteria–photosensitizer interactions, crucial for antimicrobial photodynamic therapy, is still limited due to the use of conventional imaging techniques. We present a new method for investigating the alterations in living cells and quantitatively analyzing the process of bacteria photodynamic inactivation. Digital holographic tomography (DHT) was used for in situ examination of the response of Escherichia coli and Staphylococcus aureus to the accumulation of the photosensitizers immobilized in the copolymer revealed by the changes in the 3D refractive index distributions of single cells. Obtained results were confirmed by confocal microscopy and statistical analysis.

Keywords: digital holographic tomography ; photodynamic inactivation ; single-cell bacteria

1. Introduction

The vast majority of contemporary therapeutic procedures require the use of artificial devices or implants, such as percutaneous/transdermal catheters or cannulas, percutaneous drainage, bone or tooth implants, urinary or cardiovascular stents, or cardiac valves. Such devices can be colonized by bacteria that are able to form difficult to combat biofilms and therefore create a biologically critical interface issue. The formation of microbial biofilms, i.e., on catheters, increases the risk of occurrence of bloodstream infections [1]. According to the NIH (National Institutes of Health, USA) and other reports, biofilms are involved in more than 80% of chronic inflammatory and infectious diseases, including ear infections, gastrointestinal ulcers, urinary tract infections, or pulmonary infections in cystic fibrosis patients [2][3]. Biofilms are difficult to eradicate with common antimicrobial agents because they can be nearly 1500-fold more resistant to antibiotics than planktonic, free-floating cells, and so the concept of biofilm-related diseases has been recently introduced in the medical field [4][5]. The COVID-19 pandemic caused by the Severe Acute Respiratory Syndrome Coronavirus 2 (SARS-CoV-2) has shown that bacteria-related chronic inflammatory and infectious diseases (particularly pulmonary infections) can be responsible for higher mortality [6]. It was reported that during the SARS-CoV-2 pandemic, 50% of the patients with COVID-19 who died had secondary bacterial infections [7]. The formation of biofilms on the inner and outer surfaces of the tracheal cannula, which increases the risk of ventilator-associated pneumonia, was reported [8][9]. The most common infections are caused by opportunistic pathogens, considered non-pathogenic, such as *Staphylococcus* spp., which are part of the resident flora.

Bacterial colonization by *S. aureus* on external bone fixators pins [10][11] as well as contamination of wounds by *E. coli* biofilms [12] have been reported. Bacterial biofilm formation is a multistep process in which microorganisms attach to and grow on a surface with the production of an extracellular matrix, mainly polysaccharides, and proteins. Biofilm formation takes place in three stages: attachment of bacteria to a surface, maturation, and dispersion-shedding of parts of the biofilm into the aqueous medium [13]. In this study, two biofilm-forming bacterial species were used: *E. coli* and *S. aureus*. Within 2 h, *S. aureus* could attach to the surface, which proceeded with biofilm gene expression [14]. Within 6–8 h, the biofilm completed initial proliferation and entered the maturation stage [15]. Similar times were observed for *E. coli* biofilm formation, with mature biofilm typically formed within 24 h [16].

So far, the most effective method of eliminating a potential bacterial infection revealed to have formed biofilm on a medical device has been its removal, followed by systematic and/or local antibiotics therapy [17]. Additionally, a variety of topical skin disinfectants can be applied to avoid transcutaneous contamination [18]. In some studies, a combination of at least two antimicrobial agents was found to be effective in reducing the incidence of pin-tract infection, e.g., chlorhexidine and silver sulphadiazine [19]. Studies have shown that, e.g., polyhexamethylene biguanide is effective against a diverse range of bacteria, including *Staphylococcus aureus*, methicillin-resistant *S. aureus, S. epidermidis*, *P. aeruginosa*, *E. coli*, and *K. pneumoniae*, which are common microorganisms present on infected pins [20]. However, because one of the side effects

of polyhexamethylene biguanide is a contact allergy, it is therefore often listed as a contraindication in patients at high risk [21]. The majority of antibacterial agents are available in aqueous form and are applied/administered by spraying or soaking; they remain in the target area for a very short time after application. Therefore, novel antimicrobial materials with long-term activity is a potential route for reducing the occurrence or even completely limiting bacteria biofilm formation and wound infections. There are many wound exudate rheology modifiers available for application in wound care, but the recent trends favor multifunctional polymers, especially those with antimicrobial and antifilm-forming properties.

By providing a novel diagnostic tool and a method of antibacterial photoactive material's characterization on single bacteria cell level by digital holographic tomography (DHT), the present study attempts to address some of the problems related to biofilm formation. This novel quantitative phase-imaging technique [22] is based on optical diffraction tomography, which enables the characterization of morphological, optical, and biochemical properties with a sub-micrometer [23][24][25] or even sub-nanometer resolution [26]. The theoretical lateral and axial resolution of the DHT systems are equal to 124 nm and 397 nm, respectively [27][28]. In this technique, the phase and amplitude of the scattered light waves are retrieved from the series of digital holograms registered at different angles of the illuminating beam and are then processed for the reconstruction of the three-dimensional (3D) refractive index (RI) maps or tomograms. The variation of the local RI values is associated with the examined object morphology but also with local fluctuations of its density, dependent on the chemical composition. Digital holographic tomography is based on a limited-angle holographic tomography [22][26][29][30][31] approach, which is one of the most popular versions of optical diffraction tomography used in the biomedical examination. Living cells are complex structures that contain numerous organelles with different refractive indices [25][32]. Even bacteria, being prokaryotic cells, exhibit variations of the refractive index value related to their internal structure (cell wall, cytoplasm, nucleoids) or to external factors. Moreover, DHT enables non-destructive, label-free 3D imaging with lower phototoxicity and no photobleaching.

Antimicrobial photodynamic therapy (APDT) involves the use of low-power lasers with appropriate wavelength to selectively kill microorganisms treated with a photosensitizer [33]. For the purpose of the current study, a new antibacterial photoactive material was developed and used to validate the potential of DHT application for the characterization of bacteria single-cell–photosensitizer interaction. Photosensitizers immobilized within a polymer matrix were used to obtain and utilize an antimicrobial photoactive material. As a polymer, the ammonium acryloyldimethyltaurate copolymer (AVC), being a rheology modifier widely used in pharmacology and dermatology, was applied [34][35][36]. The modifier is a copolymer that consists of acrylamido-2,2-dimethylpropanesulfonic acid and vinylpyrrolidone, with an alternating arrangement within the macromolecule. It is characterized by a high degree of cross-linking and exhibits strong interactions with polar solvents. AVC was selected as a polymer carrier for the porphyrins: pheophorbide a (Pheo) and chlorin e6 (Ce6) as well as for the photosensitizer for APDT. The AVC stabilizes the monomeric structure of porphyrins, and as a result, it enhances the photoactivity of the photosensitizer [37][38]. The antimicrobial efficacy was examined against two bacteria species: *E. coli* (Gram-negative) and *S. aureus* (Gram-positive). The photodynamic effect, resulting from irradiation of porphyrins, led to the photodynamic inactivation (PDI) of bacteria cells. The DHT was used to assess the efficiency of this process, as well as to visualize the accumulation of the photosensitizers inside the single living bacterial cells. Recently, it was reported that the DHT can be successfully used for the characterization of the dynamic changes of the 3D refractive-index distributions of living bacteria associated with the changes of their morphology in response to antibiotics [28]. However, based on our knowledge, this paper reports the first attempt to use DHT in the examination of a single bacteria cell's penetration by photosensitizers, to assess antimicrobial efficiency, and to visualize the photo-inactivated cells. Obtained results confirm the statistically significant differences of the averaged 3D-RI values, indicating the accumulation of the photosensitizers and the photo-inactivation of the single bacteria cells. Moreover, it was verified that DHT can be used for the evaluation of APDT efficacy at a single bacterial cell level. Therefore, it can be applied as a non-destructive, less time-consuming, and more cost-effective alternative versus other microscopic techniques conventionally used for these purposes.

2. Photoactive Materials and Photosensitizers Characterization

The representative absorption and luminescence spectra of the photosensitizers (PS) are presented in Figure 1. For each photosensitizer, the relevant spectral bands (Figure 1A) were used for photodynamic inactivation (PDI) of bacteria, and the photodynamic diagnosis (PDD) spectral bands were used to determine the efficiency of cells' penetration by PSs.

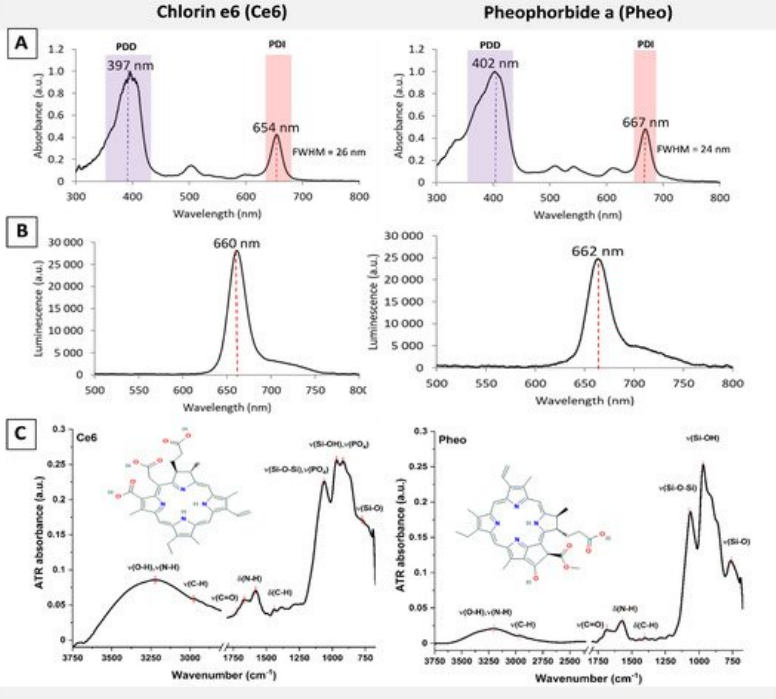

Figure 1. The characterization of the PS's absorption (**A**) and luminescence spectra (**B**) for excitation at 405 nm with central wavelengths and full width at half maximum (FWHM) of spectral bands, and (**C**) attenuated total reflectance—Fourier transform infrared (ATR-FTIR) spectra of PSs in PBS buffer deposited on the silica glass surfaces.

The reference ATR-FTIR spectra of both PSs used in further experiments are shown in Figure 1C. Ce6 and Pheo exhibit the typical absorption bands of porphyrins [39][40][41]. The broad absorption band at ~3250 cm^{-1} is attributed to O-H and N-H stretching vibrations, while weak bands in the range 3000–2800 cm^{-1} relate to stretching vibrations of C-H groups.

In the range of 1750–1500 cm^{-1}, bands arising from the stretching and deformation vibration of CO groups are observed, and in the range of approximately 1690–1575 cm^{-1}, bands of NH groups are observed. The spectral region between 1200 and 700 cm^{-1} is dominated by glass signal due to a very thin layer of deposited dyes, as well as due to phosphate bands from PBS buffer. The wavelength (655 nm) of the laser used for photoexcitation (Figure 1B) was in the range of determined FWHM of the PDI bands. The absorption spectra (Figure 1A) of the photoactive materials (AVC-Ce6, AVC-Pheo) were analogous for PSs in the PBS buffer.

After laser irradiation (λ = 655 nm) for 2 min, significant changes in the spectrum shape were observed for both types of PSs. However, the most evident modifications were observed for Ce6. The exposition of the Ce6 to the laser radiation caused a severe distortion of the porphyrin structure. The most noticeable is a redshift (toward lower wavenumber values, longer wavelengths) of the band arising from the bending vibrations of amine (N-H) at 1573 cm^{-1}, whilst simultaneously changing in the intensity of carbonyl (C = O) signals at 1690 and 1660 cm^{-1}. These bands can be assigned to the C = O stretching mode of the free and coordinated 9-keto groups [42].

In the case of Pheo, only a slight red shift for δ(NH) band is observed. Moreover, an analysis within the high-frequency range clearly showed that Ce6 was the more efficient source of reactive oxygen species (ROS). The maximum position of the combined water OH stretching and NH stretching band was shifted to higher wavenumber (i.e., higher energy and higher frequency) toward longer wavelengths approximately 120 cm^{-1} and 90 cm^{-1} for Ce6 and Pheo, respectively. This blue shift is caused by hydrogen bonds breaking and the formation of ROS, such as hydroxyl radicals [43][44].

Although ATR-FTIR spectra of AVC material are dominated by bands of ammonium acryloyldimethyltaurate/vinylpyrrolidone copolymer, some spectral features allow the assumption that PS's molecules are attached to the surface. The subtle broadening of δ(NH) and ν(CO) bands in the range of 1800–1500 cm^{-1}, as well as the presence of additional bands at ~1740 and 1400 cm^{-1}, corresponding to ester C = O and C-C aromatic groups, are detected. The position of the C = O stretching band in both AVC–PS spectra is located at higher wavenumbers than in the corresponding spectra of non-bound PSs and appears at the typical ester range. As expected, the irradiation process did not affect the AVC.

3. Qualitative and Quantitative Analysis of the Single Cells' RI Variations

Caused by Photosensitizer Penetration

The RI value is closely related to the mass concentration in biological samples [45]. According to the proposed approach, the penetration of cells by PSs is accompanied by a change of the cell's density, which leads to the increase of the single cell's RI values. To confirm this assumption, an analysis of the variation of average RI values of the single cells incubated on AVC material and photoactive material (AVC-Ce6, AVC-Pheo) was performed. The exemplary results for *E. coli* cells grown on AVC material and the representation of RI data processing are shown in Figure 2.

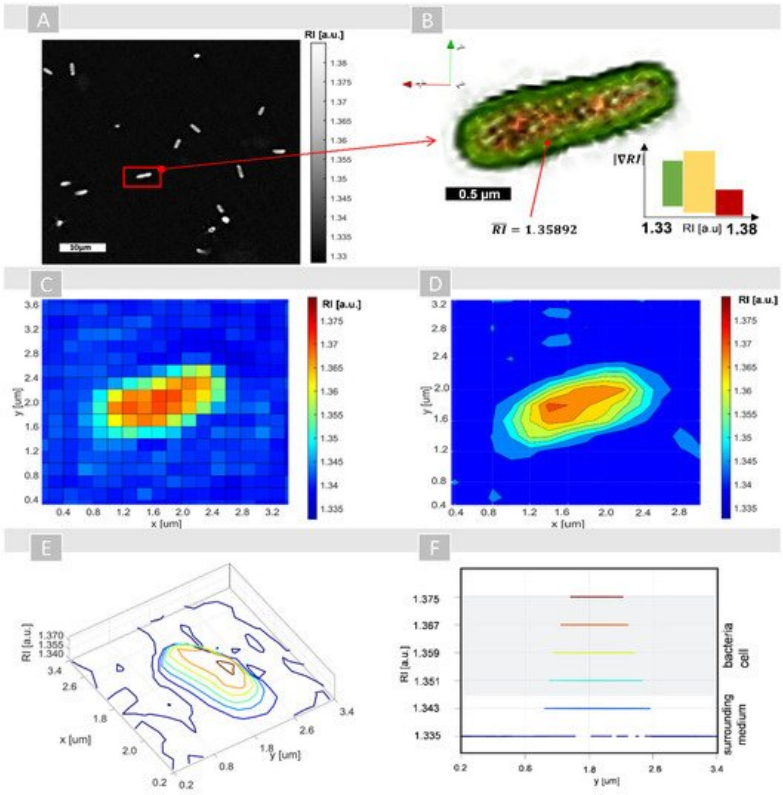

Figure 2. The exemplary results for *E. coli* cell on AVC material (non-photoactive): (**A**) reconstructed 2D-RI map (raw-data) with *E. coli* cells on the surface of AVC material; (**B**) 3D rendered and digitally stained single cell; (**C**) averaged 3D-RI distribution of single cell from all 2D-RI maps (slices) on which the cells were present; (**D**) distribution of averaged 3D-RI isolines; (**E**) pseudo-3D representation of averaged RI distribution; (**F**) cross-section of the isolines for different averaged 3D-RI values corresponding to the region occupied by a single cell.

The numerically reconstructed 3D-RI distributions contained a series of 2D-RI maps (see Figure 2A), which were used for 3D rendering and digital staining of the cells based on their RI values (see Figure 2B). Green color corresponds to the outer regions of bacteria cells (cell wall and membranes), while yellow and red colors correspond to the cell interior (cytoplasm, nucleoids, ribosomes, etc.). After segmentation, it is possible to extract the region occupied by the cell in all slices of the 3D-RI distribution by selecting the voxels that have RI higher than a specific value corresponding to the RI of the medium. Then, the averaged RI values were determined by averaging RI values from pixels of the cells' region from each 2D-RI map (slice), which enabled the 2D representation of the 3D-RI distribution of single cells (Figure 2C). However, due to the limited sampling conditions (wavelength of the used light source and resolution of the used detector) affecting the analysis of the intracellular spatial variations of the RI values, the additional processing of RI data had to be applied. The use of isolines corresponding to the planes of equal values of the RI inside the cell (see Figure 2D,E) were determined and enabled a more precise examination of the RI changes, revealing local variations of the intracellular density. Such representation of the RI data demonstrates that digital staining based on the local changes of RI values enables the direct localization of single cells and distinguishes the region occupied by a single cell from the surrounding medium (see Figure 2F).

A significant variation of the RI values from 1.3350 (corresponding to NaCl RI) to 1.3390 of the surrounding medium was documented and related to the interaction of AVC material with NaCl, leading to the local density variation. The additional measurement of the RI of AVC material with NaCl solution on the Abbe refractometer confirmed this observation, where the averaged RI was equal to 1.3371. Based on the performed analysis, it was possible to determine the range of RI values' variation inside the region occupied by a single cell: 1.34721–1.37891 for *E. coli* and 1.3512–1.38921 for *S. aureus*. The results obtained for *E. coli* correspond to the results from the alternative DHT technique, which were reported

recently [28]. The averaged 3D-RI of *E. coli* cells, in this case, was equal to 1.35892, and the standard deviation was equal to 0.00189, while for *S. aureus* these values were 1.34988 and 0.00101, respectively.

However, the direct estimation of the border value of RI indicating the boundaries between the surrounding medium and cell is a subject of considerable uncertainty. The outer cell's structures include not only the cell envelope consisting of cell wall (20–80 nm thick for Gram-positive and 1.5–10 nm for Gram-negative) and plasma membrane (about 7.5 nm thick) but also flagella and pili (or fimbriae) responsible for bacteria motility, adhesion, uptake, and excretion of proteins and DNA [46][47][48]. Structurally, bacterial flagella are long structures (3 to 12 µm), with a diameter in the range from 12 to 30 nm, while pili are 0.3–1.0 µm in length and about 7 nm in diameter. Therefore, the size of these structures (thickness, diameter) is below the lateral resolution of the DHT, and it is not possible to distinguish them from the medium. In consequence, the RI value near the cell will be subject to local variation caused by the random locations of these structures in the medium surrounding the cell and local changes of the density, which limit the determination of the boundary value of the RI that allows the region of the cell and external medium to be directly distinguished. The RI of these regions can be treated as an averaged value of the higher RI flagella/pili and lower RI of the surrounding medium. Moreover, the outer regions of bacterial cells consist of cell walls, membranes, or capsules that exhibit some permeability necessary for uptake of dissolved nutrients. The plasma membrane enables the transport of the nutrients based on facilitated diffusion, active transport, and group translocation, which can lead to local changes of the density of peripheral regions of the cell during the opposite transport of substrates to the concentration gradient from the external environment (external medium with lower RI) to the cellular interior with higher RI. In our opinion, the above reasons may explain the lower RI values in the peripheral region of the bacteria cells.

Moreover, in the context of the determined averaged RI of bacteria cells, it should be pointed out that these values correspond to the average RI of a single cell and variation of the RI values inside the single cell, however not to the averaged RI of multiple cells suspension, as mainly reported in previous studies based on immersion refractometry [49][50]. Nonetheless, as it will be shown in Section 2.4, during the reproduction process the RI distribution of single cells is significantly changing. Therefore, the determined RI of the cell's suspension will never be an averaged value of all cells with the same RI distribution because cells at different stages of cell development will be present in the same suspension. There were also some reports on determination of the RI of single bacteria cell by optofluidic immersion refractometry [51], where the averaged RI of a single cell was determined by appropriately matching the RI of the media in which the cells were suspended. However, the RI values of the subcellular structures such as cytoplasm and nucleoid [50] are changing depending on the kind of medium used [32]. Additionally, the already reported results of using optical diffraction tomography to reconstruct the 3D-RI distributions of the microalgae [24], eukaryotic cells [52], and their internal structures [32]—chromosomes, cytosol, cell membrane—confirm our concerns because, depending on the type of nutrient medium, osmolality, temperature, or fixation procedures [53], significant variation of the RI values was observed. Therefore, the use of the DHT or quantitative phase imaging for characterization of single bacteria cells requires standardization and strict control of the cell's culturing and measurement conditions to obtain comparable and repeatable results.

For the determination of the bacteria cells' penetration by examined photosensitizers (Ce6, Pheo) the dark-controls of AVC-Ce6/AVC-Pheo materials and only AVC material were used to define the change of the refractive index of the single cells caused by the accumulation of the photosensitizers. This change was estimated by the difference between the averaged refractive index of all cells incubated on AVC material (reference) and photoactive materials (AVC-Ce6/AVC-Pheo). Results are shown in Figure 3

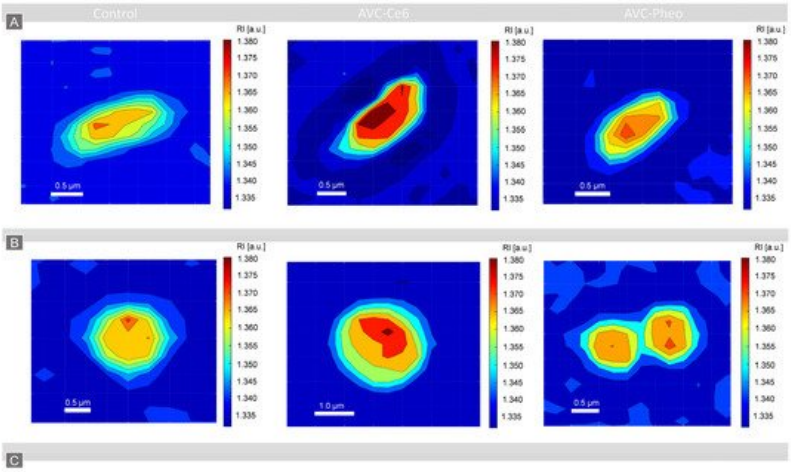

Material	AVC-Ce6		AVC-Pheo	
Bacteria species	*E. coli*	*S. aureus*	*E.coli*	*S. aureus*
Number of analyzed cells	279	301	320	330
ΔRI [a.u.]	0.01373	0.00877	0.00598	0.00497
Standard deviation [a.u.]	0.00049	0.00091	0.00054	0.0085

Figure 3. The representative 2D-RI maps of single *E. coli* (**A**) and *S. aureus* (**B**) cells on AVC (control), AVC-Ce6, AVC-Pheo materials and the averaged RI differences with standard deviations (**C**).

For all examined bacteria species and the photoactive materials, an increase of the averaged RI of single cells was observed. In case of the AVC-Ce6 material, more substantial changes of the RI were noted for *E. coli* cells than for *S. aureus*. Moreover, a greater difference of the averaged RI values was observed for these two bacteria species in the case of AVC-Ce6 material than in AVC-Pheo. Obtained results indicate considerably more change in averaged RI of single cells for AVC-C6 material.

In our approach, we assumed that the greater change of the averaged RI of cells indicated a more effective accumulation of the photosensitizer inside the bacteria cell. To determine whether the observed changes of the averaged RI of cells caused by PS penetration were statistically significant, a one-way ANOVA was performed. To obtain a representative set of data for this analysis, at least 279 cells of each species were examined. The normality assumption of the average RI values of single cells was confirmed by the Anderson–Darling test at 5% significance level. The estimated *p*-value for the *F*-statistic is significantly smaller (6.159×10^{-32}) than the significance level (0.05), which means that the test rejected the null hypothesis that all group means were equal. It indicates that there exists a statistically significant difference between the analyzed groups corresponding to the averaged RI values of bacteria cells (*E. coli, S. aureus*) on AVC, AVC-Ce6, and AVC-Pheo materials. Moreover, the variability between groups was higher than the variability within the groups. Obtained results of the ANOVA indicate that the presence of the photosensitizers in the AVC material significantly influenced the averaged RI value of the single cells. Therefore, the performed examination indicated that the analysis of the 3D-RI distribution of single bacterial cell could be used for characterization of the sub-micrometer local changes of the intercellular density associated with the accumulation of the photosensitizers inside the single cells.

To confirm that the change of the averaged RI of the bacteria cells incubated with photoactive material is related to the effectiveness of the cell's penetration by the photosensitizer, an additional examination was performed by means of scanning fluorescence confocal microscopy. The *E. coli* and *S. aureus* cells incubated for 8 h with the photosensitizer were examined to prove whether photosensitizers were accumulating in the cell's wall or inside of the cell. After photoexcitation of the photosensitizers by the laser light with a wavelength equal to 405 nm (corresponding to the PDD absorption bands of both photosensitizers), fluorescence images of single cells, were registered (see Figure 4).

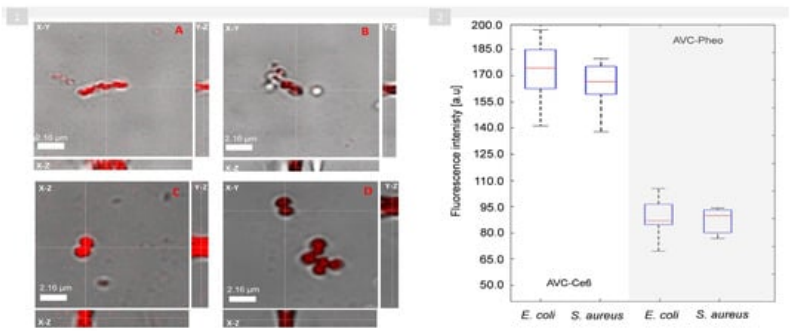

Figure 4. (**1**) Representative confocal 2D microscopic images (combined DIC-fluorescence images) of *E. coli* cells penetrated by Ce6 (**A**), Pheo (**B**), and *S. aureus* cells penetrated by Ce6 (**C**) and Pheo (**D**) photosensitizers; (white-dashed lines indicate the planes for which the axial (X-Z, Y-Z) cross-sections (Δz = 3μm, with resolution: 0.04 μm) were extracted). (**2**) The boxplot representing the variation of the fluorescence intensity in the region of single cells.

The analysis of the differential interference contrast (DIC) and fluorescence images of cells as well as axial cross-sections (X-Z, Y-Z) resulted in the observation that the fluorescence signal is spatially overlapping all-regions occupied by the bacterial cells—not only in the cells' capsule, cell wall, or cytoplasm membrane, but also inside of the cells of both bacteria species (Gram-positive and Gram-negative). The results indicate the presence of photosensitizers inside the cells, which confirms the ability of the used photosensitizers to penetrate through the bacterial cell's wall into the cell of both examined species (Gram-positives and Gram-negatives). Anionic PSs such as Ce6 are not taken up into bacterial cells via simple diffusion. Uptake of anionic PS may be mediated through a combination of electrostatic charge interaction and by protein transporters, and Pheo (cationic PS) transport is mediated by electrostatic interactions and self-promoted uptake pathways. This pathway involves the binding of the cationic molecules to the outer membrane, which is rich in lipopolysaccharides (LPS), resulting in the progressive displacement of divalent cations (both Ca^{2+} and Mg^{2+} stabilize the LPS structure via electrostatic bonds), thereby weakening the outer membrane. The destabilization of the LPS layer results in the progressive weakness of the permeability barrier. The presence of cationic dye in the AVC material results in the widening of the crack in the LPS layer [54]. Efflux pumps are bacterial transport proteins that are involved in extrusion of substrates from the cellular interior to the external environment. Pheo is a natural product identified as an efflux pump inhibitor (EPI) [55][56].

It was proven that it is possible to photodynamically inactivate Gram-negative bacteria without photosensitizer accumulation in the bacterial cells. This fact is especially interesting, considering that the development of resistance may be prevented, leaving the active components (PS) outside the bacterium [57]. However, the fluorescence intensity of the obtained images indicates that the penetration of both bacteria species cells is more effective in the case of the Ce6 than Pheo photosensitizer. Moreover, the comparison of the fluorescence signal intensity (see Figure 4(1)) revealed that the concentration of the Pheo photosensitizer inside the cells is significantly lower than in the case of theCe6, which indicates the significantly lower penetration of the cell by this photosensitizer. These observations were also confirmed by the analysis of the discrete fluorescence intensity of single *E. coli* and *S. aureus* cells (see Figure 4(2)), demonstrating the higher fluorescence intensity in the case of the AVC-Ce6 material, which corresponds to the accumulation and concentration of the photosensitizers inside the cells. These results are consistent across the changes in the average RI of examined cells because, for AVC-Pheo material, the fluorescence intensity was significantly lower than for AVC-Ce6 material (see Figure 3). Therefore, the high correlation of the changes of the RI value of the cells, along with the efficiency of the cells' penetration by examining photosensitizers, proved the capability of digital holotomography in the characterization of local density changes in single cells. Moreover, these results indicate that during the excitation of accumulated photosensitizer by light with a wavelength of 655 nm used to get the photodynamic inactivation, the generated free radicals destroy not only the bacterial membranes (cell wall, cytoplasm membrane) but also most probably the nucleoids present inside the cell.

4. Photodynamic Inactivation of Bacteria Cells Revealed by DHT and Its Quantitative Analysis

The holotomographic technique was used to record a series of digital holograms and reconstruct the 3D-RI maps. As it was confirmed in the previous section, the bacterial cells have different averaged RI values due to interaction with different photoactive materials, which makes this method suitable for bacteria cells visualization and characterization of cell penetration. In this section, the results of the examination of the induced photodynamic inactivation of bacterial cells are presented and based on RI-data provided by DHT. In total, six samples—AVC (dark-control), AVC (bright-control), AVC-C6 (dark-control), AVC-Ce6 (photoexcited), AVC-Pheo (dark-control), AVC-Pheo (photoexcited)—were prepared in eight replicates and were examined. Firstly, after segmentation of the representative 2D-RI maps, the binary masks indicating the regions of single cells were generated and used to count number of cells on the surface of the AVC materials 8 and 24 h after photoexcitation. The exemplary reconstructed 2D-RI maps are depicted in Figure 5.

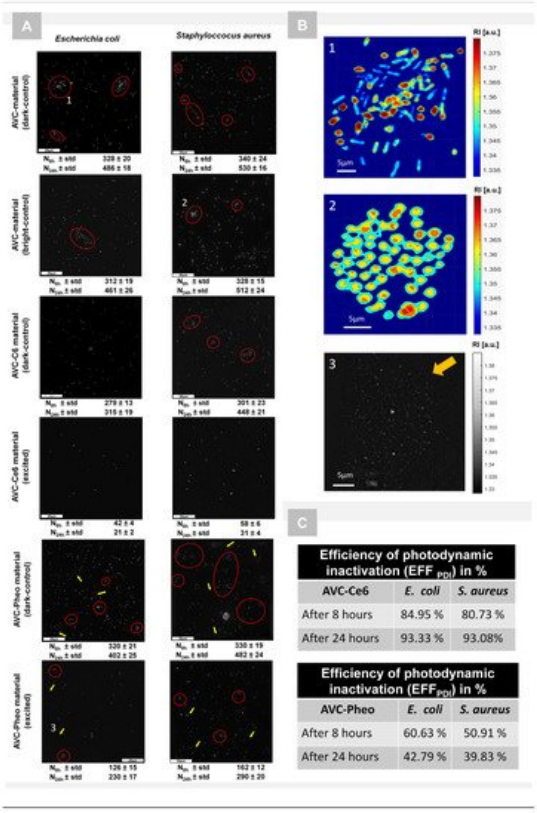

Figure 5. (**A**) Representative 2D-RI maps of *E. coli* and *S. aureus* cells grown on the surface of three kinds of AVC materials (24 h after photodynamic treatment) mean values of the cells' number (N_{8h}, N_{24h}) and its standard deviation 8 and 24 h after photoexcitation. (Red ellipses indicate the bacterial cells clusters characteristic for biofilm formation; yellow arrows indicate the photosensitizer's aggregates in the material). (**B**) The exemplary enlarged 2D-RI maps of characteristic structures (cells clusters—(**1**,**2**); aggregates—(**3**)) indicated on (**A**). (**C**) The efficiency of the photodynamic inactivation EFF_{PDI} (detailed description in Section 4.8).

Obtained results demonstrate that in both dark- and bright-control samples of AVC material, an increase in the bacterial cells number occurred, which indicates that the used AVC may deliver some nutrients enabling bacterial cell reproduction. Moreover, the laser illumination did not affect the growth of the bacterial cells on the surface of this material. The reproduction rate is slightly higher for *S. aureus* than *E. coli* bacteria.

In the case of the AVC-Ce6 dark-control after 8 h of incubation, the number of bacteria cells was comparable with the number of cells of AVC without photosensitizer. However, after 24 h a decrease in the number of cells was observed for both bacteria species. As in the previous case, the division of *S. aureus* was higher than *E. coli*, which was also confirmed by the presence of the clusters of cells characteristic for biofilm formation. The analysis of photoexcited samples indicated a significant decrease in the cells' number for both species. Obtained results confirm high (nearly 80–85% after 8 h and over 93% after 24 h) photo-inactivation efficiency of Ce6. Moreover, the results obtained for dark-control proved that photosensitizer exhibited antimicrobial properties even without photoexcitation, but the effect of the cells' number decrease was substantially weaker.

In the case of the AVC-Pheo material without the photoexcitation, the decrease of the number of cells and photo-inactivation efficiency was significantly lower than in the case of the Ce6 photosensitizer, and the same tendency of lower efficiency for *S. aureus* species was observed. In the case of the photoexcited materials, the decrease of the cells' number was observed; however, it was considerably lower than in the case of Ce6. Moreover, after 24 h the number of cells was nearly doubled in comparison with the samples after 8 h of incubation, which indicates that cells present on the material surface after 8 h were not inactivated. Obtained results show that Pheo exhibited antimicrobial properties, but its efficiency was substantially lower than in the case of Ce6. Furthermore, in the case of both dark/bright samples and for both species, cell clusters were present, indicating the possible formation of bacterial biofilm. Infrared spectroscopy confirmed that Ce6 was the more efficient source of reactive oxygen species than Pheo, which has been proven to exert antimicrobial action [58]. Moreover, the limited antimicrobial efficiency of the Pheo may be caused by its aggregation because within some regions of the reconstructed 2D-RI maps it was possible to distinguish areas of different RI values (see Figure 5B), indicating local changes of the density caused by some inhomogeneity of the material, probably associated with the presence of the Pheo aggregates. It was reported that Pheo undergoes aggregations in an aqueous solution, while Ce6 remains monomeric in water [59]. Uncontrolled aggregation of photosensitizer may significantly affect

photodynamic inactivation due to the weaker cells' penetration by Pheo and inefficient photoexcitation leading to the low generation rate of free radicals.

This observation was confirmed by obtained results of confocal microscopic examination (see Figure 4), where the significantly lower fluorescence intensity was detected for Pheo and was associated with the photosensitizer's aggregation process. The accumulation of the PS can also be responsible for the considerably smaller changes of the averaged RI values of all bacteria cells grown on the surface of AVC-Pheo material.

References

1. Jamal, M.A.; Garoge, K.; Rosenblatt, J.S.; Hachem, R.Y.; Raad, I.I. Development of Gendine-Coated Cannula for Continuous Subcutaneous Insulin Infusion for Extended Use. Antimicrob. Agents Chemother. 2015, 59, 4397–4402.
2. Römling, U.; Balsalobre, C. Biofilm infections, their resilience to therapy and innovative treatment strategies. J. Intern. Med. 2012, 272, 541–561.
3. Vestby, L.K.; Grønseth, T.; Simm, R.; Nesse, L.L. Bacterial Biofilm and Its Role in the Pathogenesis of Disease. Antibiot. 2020, 9, 59.
4. Del Pozo, J.L. Biofilm-related disease. Expert Rev. Anti-Infect. Ther. 2018, 16, 51–65.
5. Jamal, M.; Ahmad, W.; Andleeb, S.; Jalil, F.; Imran, M.; Nawaz, M.A.; Hussain, T.; Ali, M.; Rafiq, M.; Kamil, M.A. Bacterial biofilm and associated infections. J. Chin. Med. Assoc. 2018, 81, 7–11.
6. Chen, N.; Zhou, M.; Dong, X.; Qu, J.; Gong, F.; Han, Y.; Qiu, Y.; Wang, J.; Liu, Y.; Wei, Y.; et al. Epidemiological and clinical characteristics of 99 cases of 2019 novel coronavirus pneumonia in Wuhan, China: A descriptive study. Lancet 2020, 395, 507–513.
7. Zhou, F.; Yu, T.; Du, R.; Fan, G.; Liu, Y.; Liu, Z.; Xiang, J.; Wang, Y.; Song, B.; Gu, X.; et al. Clinical course and risk factors for mortality of adult inpatients with COVID-19 in Wuhan, China: A retrospective cohort study. Lancet 2020, 395, 1054–1062.
8. Póvoa, H.C.C.; Chianca, G.C.; Iorio, N.L.P.P. COVID-19: An Alert to Ventilator-Associated Bacterial Pneumonia. Infect. Dis. Ther. 2020, 9, 417–420.
9. Bao, L.; Zhang, C.; Dong, J.; Zhao, L.; Li, Y.; Sun, J. Oral Microbiome and SARS-CoV-2: Beware of Lung Co-infection. Front. Microbiol. 2020, 11, 1840.
10. Wickens, D.J.; West, G.; Kelly, P.J.; Verran, J.; Lynch, S.; Whitehead, K.A. Antimicrobial Activity of Nanocomposite Zirconium Nitride/Silver Coatings to Combat External Bone Fixation Pin Infections. Int. J. Artif. Organs 2012, 35, 817–825.
11. Walker, J. Pin site infection in orthopaedic external fixation devices. Br. J. Nurs. 2012, 21, 148–151.
12. Jennison, T.; McNally, M.; Pandit, H. Prevention of infection in external fixator pin sites. Acta Biomater. 2014, 10, 595–603.
13. Rabin, N.; Zheng, Y.; Opoku-Temeng, C.; Du, Y.; Bonsu, E.; Sintim, H.O. Biofilm formation mechanisms and targets for developing antibiofilm agents. Futur. Med. Chem. 2015, 7, 493–512.
14. Boudjemaa, R.; Steenkeste, K.; Canette, A.; Briandet, R.; Fontaine-Aupart, M.-P.; Marlière, C. Direct observation of the cell-wall remodeling in adhering Staphylococcus aureus 27217: An AFM study supported by SEM and TEM. Cell Surf. 2019, 5, 100018.
15. Gutiérrez, D.; Hidalgo-Cantabrana, C.; Rodríguez, A.; García, P.; Ruas-Madiedo, P. Monitoring in Real Time the Formation and Removal of Biofilms from Clinical Related Pathogens Using an Impedance-Based Technology. PLoS ONE 2016, 11, e0163966.
16. Wang, Y.; Reardon, C.P.; Read, N.; Thorpe, S.; Evans, A.; Todd, N.; Van Der Woude, M.; Krauss, T.F. Attachment and antibiotic response of early-stage biofilms studied using resonant hyperspectral imaging. npj Biofilms Microbiomes 2020, 6, 1–7.
17. Harris, L.G.; Richards, R.G. Staphylococci and implant surfaces: A review. Injury 2006, 37, S3–S14.
18. Rozbruch, S.R.; Kazmers, N.H.; Fragomen, A.T. Prevention of pin site infection in external fixation: A review of the literature. Strat. Trauma Limb Reconstr. 2016, 11, 75–85.
19. Ogbemudia, O.A.; Bafor, A.; Edomwonyi, E.; Enemudo, R. Prevalence of pin tract infection: The role of combined silver sulphadiazine and chlorhexidine dressing. Niger. J. Clin. Pr. 2010, 13, 268–271.
20. Lee, C.K.; Chua, Y.P.; Saw, A. Antimicrobial Gauze as a Dressing Reduces Pin Site Infection: A Randomized Controlled Trial. Clin. Orthop. Relat. Res. 2012, 470, 610–615.

21. Sukakul, T.; Dahlin, J.; Pontén, A.; Antelmi, A.; Bruze, M.; Hamnerius, N.; Hauksson, I.; Isaksson, M.; Lejding, T.; Svedman, C. Contact allergy to polyhexamethylene biguanide (polyaminopropyl biguanide). Contact Dermat. 2020, 84, 326–331.

22. Park, Y.; Depeursinge, C.; Popescu, G. Quantitative phase imaging in biomedicine. Nat. Photon. 2018, 12, 578–589.

23. Kim, K.; Yoon, J.; Shin, S.; Lee, S.; Yang, S.-A.; Park, Y. Optical diffraction tomography techniques for the study of cell pathophysiology. J. Biomed. Photon. Eng. 2016, 2, 020201–1.

24. Jung, J.; Hong, S.-J.; Kim, H.-B.; Kim, G.; Lee, M.; Shin, S.; Lee, S.; Kim, D.-J.; Lee, C.-G.; Park, Y. Label-free non-invasive quantitative measurement of lipid contents in individual microalgal cells using refractive index tomography. Sci. Rep. 2018, 8, 1–10.

25. Kim, T.-K.; Lee, B.-W.; Fujii, F.; Kim, J.K.; Pack, C.-G. Physicochemical Properties of Nucleoli in Live Cells Analyzed by Label-Free Optical Diffraction Tomography. Cells 2019, 8, 699.

26. Cotte, Y.; Toy, F.M.; Jourdain, P.; Pavillon, N.; Boss, D.; Magistretti, P.J.; Marquet, P.; Depeursinge, C. Marker-free phase nanoscopy. Nat. Photon. 2013, 7, 113–117.

27. Lauer, V. New approach to optical diffraction tomography yielding a vector equation of diffraction tomography and a novel tomographic microscope. J. Microsc. 2002, 205, 165–176.

28. Oh, J.; Ryu, J.S.; Lee, M.; Jung, J.-H.; Han, S.; Chung, H.J.; Park, Y. Three-dimensional label-free observation of individual bacteria upon antibiotic treatment using optical diffraction tomography. Biomed. Opt. Express 2020, 11, 1257–1267.

29. Kuś, A.; Krauze, W.; Makowski, P.L.; Kujawińska, M. Holographic tomography: Hardware and software solutions for 3D quantitative biomedical imaging (Invited paper). ETRI J. 2019, 41, 61–72.

30. Kuś, A.; Krauze, W.; Kujawinska, M. Limited-angle holographic tomography with optically controlled projection generation. In Proceedings of the Three-Dimensional and Multidimensional Microscopy: Image Acquisition and Processing XXII, San Francisco, CA, USA, 9 March 2015; Volume 9330, p. 933007.

31. Kus, A.; Krauze, W.; Kujawinska, M. Active limited-angle tomographic phase microscope. J. Biomed. Opt. 2015, 20, 111216.

32. Kim, T.-K.; Lee, B.-W.; Fujii, F.; Lee, K.-H.; Lee, S.; Park, Y.; Kim, J.K.; Lee, S.-W.; Pack, C.-G. Mitotic Chromosomes in Live Cells Characterized Using High-Speed and Label-Free Optical Diffraction Tomography. Cells 2019, 8, 1368.

33. Koshi, E.; Mohan, A.; Rajesh, S.; Philip, K. Antimicrobial photodynamic therapy: An overview. J. Indian Soc. Periodontol. 2011, 15, 323–327.

34. Gouveia, T.H.N.; De Souza, D.F.S.; Aguiar, F.H.B.; Ambrosano, G.M.B.; Lima, D.A.N.L. Effect of ammonium acryloyldimethyltaurate copolymer on the physical and chemical properties of bleached dental enamel. Clin. Oral Investig. 2019, 24, 2701–2711.

35. Daneluz, J.; Favero, J.D.S.; Dos Santos, V.; Weiss-Angeli, V.; Gomes, L.B.; Mexias, A.S.; Bergmann, C.P. The Influence of Different Concentrations of a Natural Clay Material as Active Principle in Cosmetic Formulations. Mater. Res. 2020, 23, 23.

36. Nigro, F.; Cerqueira, C.; Rossi, A.; Cardoso, V.; Vermelho, A.B.; Ricci-Júnior, E.; Dos Santos, E.P.; Mansur, C.R.E. Development, characterization and in vitro toxicity evaluation of nanoemulsion-loaded hydrogel based on copaiba oil and coenzyme Q10. Colloids Surf. A Physicochem. Eng. Asp. 2020, 586, 124132.

37. Marta, K.; Iwona, H.; Agnieszka, U.-J.; Igor, B.; Halina, P. Sol-gel Coated Fiberoptic Applicator for Photodynamic Medicine-Optical and AFM Characterization. Biocybern. Biomed. Eng. 2012, 32, 41–50.

38. Calori, I.R.; Caetano, W.; Tedesco, A.C.; Hioka, N. Self-aggregation of verteporfin in glioblastoma multiforme cells: A static and time-resolved fluorescence study. Dye. Pigment. 2020, 182, 108598.

39. Wawrzyńska, M.; Duda, M.; Hołowacz, I.; Kaczorowska, A.; Ulatowska-Jarża, A.; Buzalewicz, I.; Kałas, W.; Wysokińska, E.; Biały, D.; Podbielska, H.; et al. Photoactive Pore Matrix for In Situ Delivery of a Photosensitizer in Vascular Smooth Muscle Cells Selective PDT. Materials 2019, 12, 4110.

40. Yue, C.; Zhang, C.; Alfranca, G.; Yang, Y.; Jiang, X.; Yang, Y.; Pan, F.; De La Fuente, J.M.; Cui, D. Near-Infrared Light Triggered ROS-activated Theranostic Platform based on Ce6-CPT-UCNPs for Simultaneous Fluorescence Imaging and Chemo-Photodynamic Combined Therapy. Theranostics 2016, 6, 456–469.

41. Gladkova, O.; Parkhats, M.; Gorbachova, A.; Terekhov, S. FTIR spectra and normal-mode analysis of chlorin e6 and its degradation-induced impurities. Spectrochim. Acta Part A Mol. Biomol. Spectrosc. 2010, 76, 388–394.

42. Sato, H.; Ozaki, Y.; Uehara, K.; Araki, T.; Iriyama, K. ATR/FT-IR Study of a Monolayer Film of Chlorophyll-a on a Germanium Plate. Appl. Spectrosc. 1993, 47, 1509–1512.

43. Yu, J.; Wang, G.; Wang, X.; Xu, Y.; Chen, S.; Wang, X.; Jiang, L. Improving the freeze-thaw stability of soy protein emulsions via combing limited hydrolysis and Maillard-induced glycation. LWT 2018, 91, 63–69.
44. Kizil, R.; Irudayaraj, J.; Seetharaman, K. Characterization of Irradiated Starches by Using FT-Raman and FTIR Spectroscopy. J. Agric. Food Chem. 2002, 50, 3912–3918.
45. Popescu, G.; Park, Y.; Lue, N.; Best-Popescu, C.; DeFlores, L.; Dasari, R.R.; Feld, M.S.; Badizadegan, K. Optical imaging of cell mass and growth dynamics. Am. J. Physiol. Physiol. 2008, 295, C538–C544.
46. Lagage, V.; Uphoff, S. Filming flagella and pili in action. Nat. Rev. Genet. 2018, 16, 584.
47. Salton, M.R.J.; Kim, K.S. Structure-Medical Microbiology-NCBI Bookshelf. Available online: (accessed on 26 November 2020).
48. De Aldecoa, A.L.I.; Zafra, O.; González-Pastor, J.E. Mechanisms and Regulation of Extracellular DNA Release and Its Biological Roles in Microbial Communities. Front. Microbiol. 2017, 8, 1390.
49. Marquis, R.E. Immersion Refractometry of Isolated Bacterial Cell Walls. J. Bacteriol. 1973, 116, 1273–1279.
50. Valkenburg, J.A.; Woldringh, C.L. Phase separation between nucleoid and cytoplasm in Escherichia coli as defined by immersive refractometry. J. Bacteriol. 1984, 160, 1151–1157.
51. Liu, P.; Chin, L.; Ser, W.; Ayi, T.; Yap, P.; Bourouina, T.; Leprince-Wang, Y. Real-time Measurement of Single Bacterium's Refractive Index Using Optofluidic Immersion Refractometry. Procedia Eng. 2014, 87, 356–359.
52. Pour, P.A.; Kenney, M.C.; Kheradvar, A. Bioenergetics Consequences of Mitochondrial Transplantation in Cardiomyocytes. J. Am. Hear. Assoc. 2020, 9, e014501.
53. Baczewska, M.; Eder, K.; Ketelhut, S.; Kemper, B.; Kujawińska, M. Refractive Index Changes of Cells and Cellular Compartments Upon Paraformaldehyde Fixation Acquired by Tomographic Phase Microscopy. Cytom. Part. A 2020, 99, 388–398.
54. George, S.; Hamblin, M.R.; Kishen, A. Uptake pathways of anionic and cationic photosensitizers into bacteria. Photochem. Photobiol. Sci. 2009, 8, 788–795.
55. Zechini, B.; Versace, I. Inhibitors of multidrug resistant efflux systems in bacteria. Recent Pat. Anti-Infect. Drug Discov. 2009, 4, 37–50.
56. Pathania, R.; Sharma, A.; Gupta, V.K. Efflux pump inhibitors for bacterial pathogens: From bench to bedside. Indian J. Med. Res. 2019, 149, 129–145.
57. Preuß, A.; Zeugner, L.; Hackbarth, S.; Faustino, M.; Neves, M.; Cavaleiro, J.; Roeder, B. Photoinactivation of Escherichia coli (SURE2) without intracellular uptake of the photosensitizer. J. Appl. Microbiol. 2012, 114, 36–43.
58. Kowal, K.; Cronin, P.; Dworniczek, E.; Żegliński, J.; Tiernan, P.; Wawrzyńska, M.; Podbielska, H.; Tofail, S.A.M. Biocidal effect and durability of nano-TiO2 coated textiles to combat hospital acquired infections. RSC Adv. 2014, 4, 19945.
59. Roeder, B.; Wabnitz, H. Time-resolved fluorescence spectroscopy of hematoporphyrin, mesoporphyrin, pheophorbide a and chlorin e6 in ethanol and aqueous solution. J. Photochem. Photobiol. B Biol. 1987, 1, 103–113.

Retrieved from https://encyclopedia.pub/entry/history/show/24998